Cross-comparison of diagnostic and 0D modeling of a micro-hollow cathode discharge in the stationary regime in an Ar/N 2 gas mixture

Alice Remigy, Salima Kasri, Thibault Darny, Hiba Kabbara, Ludovic William, Gérard Bauville, Kristaq Gazeli, Stéphane Pasquiers, João Santos Sousa, Nelson de Oliveira, et al.

Journal of Physics D: Applied Physics

Cross-comparison of diagnostic and 0D modeling of a micro-hollow cathode discharge in the stationary regime in an Ar/N_2 gas mixture

To cite this article before publication: Alice Remigy *et al* 2021 *J. Phys. D: Appl. Phys.* in press https://doi.org/10.1088/1361-6463/ac3c74

Cross-comparison of diagnostics and 0D modeling of a Micro-Hollow Cathode Discharge in the stationary regime in an Ar/N_2 gas mixture

Alice Remigy[1], Salima Kasri[1], Thibault Darny[2], Hiba Kabbara[1], Ludovic William[1], Gérard Bauville[2], Kristaq Gazeli[2], Stéphane Pasquiers[2], João Santos Sousa[2], Nelson De Oliveira[3], Nader Sadeghi[4], Guillaume Lombardi[1], and Claudia Lazzaroni[1]

[1]Université Sorbonne Paris Nord, Laboratoire des Sciences des Procédés et des Matériaux, LSPM, CNRS, UPR 3407, F-93430, Villetaneuse, France
[2]Université Paris-Saclay, CNRS, Laboratoire de Physique des Gaz et des Plasmas, 91405 Orsay, France
[3]Synchrotron Soleil, Orme des Merisiers, St. Aubin, BP 48, CEDEX, 91192 Gif sur Yvette, France
[4]LTM (URA5129) and LIPhy (URA5588), Université Grenoble-Alpes and CNRS, Grenoble,France

Abstract

A micro-hollow cathode discharge (MHCD) operated in Ar/N_2 gas mixture, working in the normal regime, was studied both experimentally and with a 0D (volume-averaged) model in this work. This source provides high electron densities (up to 10^{15} cm^{-3}) at low injected power (1W). To understand the mechanisms leading to the production of N atoms, the densities of electrons, N atoms and argon metastable atoms (Ar*) were monitored over a wide range of experimental conditions. Electrons, N atoms and Ar* densities were probed by means of Optical Emission Spectroscopy (OES), Vacuum Ultra Violet Fourier Transform Spectroscopy (VUV FTS) and Tunable Diode Laser Absorption Spectroscopy (TDLAS), respectively. Measurements showed that using a smaller hole diameter enables to work with less injected power, while increasing the power density inside the hole and, subsequently, increasing the densities of excited species. Varying the percentage of N_2 in the gas mixture highlighted that, up to 80%, the density of N atoms increases although the dissociation rate drops. Looking at the processes involved in the production of N atoms with the help of the 0D model, we found that at very low N_2 fraction, N atoms are mostly produced through dissociative electron-ion recombination. However, adding more N_2 decreases drastically the electron density. The density of N atoms does not drop thanks to the contribution of Ar* atoms, which are the main species dissociating N_2 between 5 and 55% of N_2 in the gas mixture. A reasonable agreement is found between the experiments and the model results. This study shows that, with this MHCD, it is possible to significantly modify the production of N atoms when modifying the physical parameters, making it particularly relevant for applications requiring a N atoms source, such as nitride deposition.

1 Introduction

Microplasmas, defined by a micrometric scale of at least one of their dimensions, have drawn attention in recent years with applications in various fields, such as thin film deposition and nanomaterial synthesis [1–3], surface treatment [4, 5], sterilization [6, 7], lighting [8–10] and micro-propulsion [11]. Thanks to their small size, microplasmas can be generated at high pressure (up to atmospheric) with low injected power (1 W). Futhermore, they yield high power densities up to 100 $kW.cm^{-3}$ and even higher in some cases [12]. Those are significant advantages compared to conventional non-thermal plasma sources.

Micro Hollow Cathode Discharge (MHCD) is a particular geometry of a microplasma source. It consists of an electrode-dielectric-electrode assembly that is drilled, at least partially, with a hole between a few tens and hundreds of micrometers in diameter. It was first introduced in the 1990s by Schoenbach *et al.* [13, 14]. At very low discharge current (< 0.1 mA), the DC MHCD works in the abnormal regime where the plasma is confined inside the hole. Despite the use of DC power supply, a self-pulsing regime appears at intermediate current values (typically between 0.1 and 0.5 mA) and the plasma oscillates between the interior and the exterior of the hole. The normal regime, attained at higher currents, is characterized by an expansion of the plasma on the cathodic surface. MHCDs provide high electronic densities (up to 10^{15} cm^{-3} [15]), which is expected to yield high precursor dissociation. This would be especially suited for the production of N atoms, which are needed for many applications, among which the synthesis of novel nanomaterials [16] and large band gap nitrides such as hexagonal boron nitride (h-BN) for high power electronics [17]. To shift from the harmful nitrogen-containing precursors currently used in the industry (ammonia NH_3, borazine $B_3H_6N_3$) to molecular nitrogen (N_2), one has to overcome its high bonding energy (9.5 eV), which prevents dissociation rates higher than a few percents at low processing temperatures (< 800°C) [18]. Efforts to improve the production of nitrogen atoms (N) showed that the controlled addition of argon (Ar) in the operating gas mixture enhances the dissociation of N_2 [19, 20]. For the deposition of h-BN, our team opted for boron tribromide (BBr_3) as the boron precursor [1]. It is added downstream of the MHCD and dissociated thermally.

In this paper, we have experimentally studied the production of N atoms in a MHCD working in the normal regime, in an Ar/N_2 gas mixture. To obtain complete understanding of the chemistry at stake, a volume averaged (0D) model of the discharge was developed. The density of N atoms was monitored by means of two different absorption spectroscopy methods. The challenging Vacuum Ultra Violet (VUV) spectral range of N atoms dipole transitions (≈ 120 nm) led us to use the state-of-the-art Fourier Transform Spectrometer of the SOLEIL synchrotron. In addition, the density of argon atom metastables ($Ar(1s_5)$, hereafter denoted as Ar*) was monitored, by means of tunable diode laser absorption spectroscopy, since those species may lead to the dissociation of N_2 through the reaction $Ar^m + N_2 \rightarrow N + N + Ar$ [21]. The electronic density was probed as well, using optical emission spectroscopy (OES), to understand how the electrons (e) participate in the dissociation process.

Section 2 describes the three experimental setups as well as the 0D model employed to characterize the discharge. Section 3 discusses the influence of different experimental parameters (hole diameter, gas pressure and mixture) on the production of N atoms.

2 Experimental setup and description of the model

2.1 Plasma source

The MHCD device, schematized in figure 1a, uses alumina (Al_2O_3) as the dielectric (750 μm thick), which is placed between two molybdenum electrodes (100 μm thick each). The dielectric and electrodes are assembled together using an epoxy glue suited for high-temperature operation. A hole is drilled through the assembly using a marking laser. Three different hole diameters have been used in this study : 0.4, 1 and 2 mm. This MHCD device is placed in the reactor illustrated in figure 1b, at the junction between two vacuum chambers. A gas mixture of Ar/N_2, with varying proportions of each gas, is injected in the upstream chamber (left hand side) at a constant total flow rate of 100 sccm. A pipe links the two chambers, maintaining them at the same pressure. This pressure, ranging from 30 to 90 mbar, is regulated using a pump and manual valve, pumping in the downstream chamber (right hand side).

The MHCD is then ignited using a negative DC power supply (0-1000 V). The electrode in the upstream chamber is connected to the negative high voltage (HV) of the power supply, being thus the cathode, while the anode is connected to the ground and faces the downstream chamber, as represented in figure 1b. The electrical parameters of the discharge are monitored through two voltage probes. The first probe is located post the ballast resistor $R_b = 480$ kΩ, used to limit the discharge current, and measures the discharge voltage V_d delivered to the plasma. The second probe is used to record the voltage V_I across the 180 Ω resistor R_m, in order to measure the discharge current I_d. Because the pair (V_d,I_d) is determined by the discharge conditions, a current $I_d = 1$ mA is used as a reference, while the voltage V_d is not set by the operator and its value adapts to fit the conditions. At such discharge current, the MHCD operates in the normal regime, with continuous discharge voltage and current.

Three different optical diagnostics were used to evaluate the density of electrons, N atoms and argon metastables in the plasma, respectively, as described in sections 2.2-4.

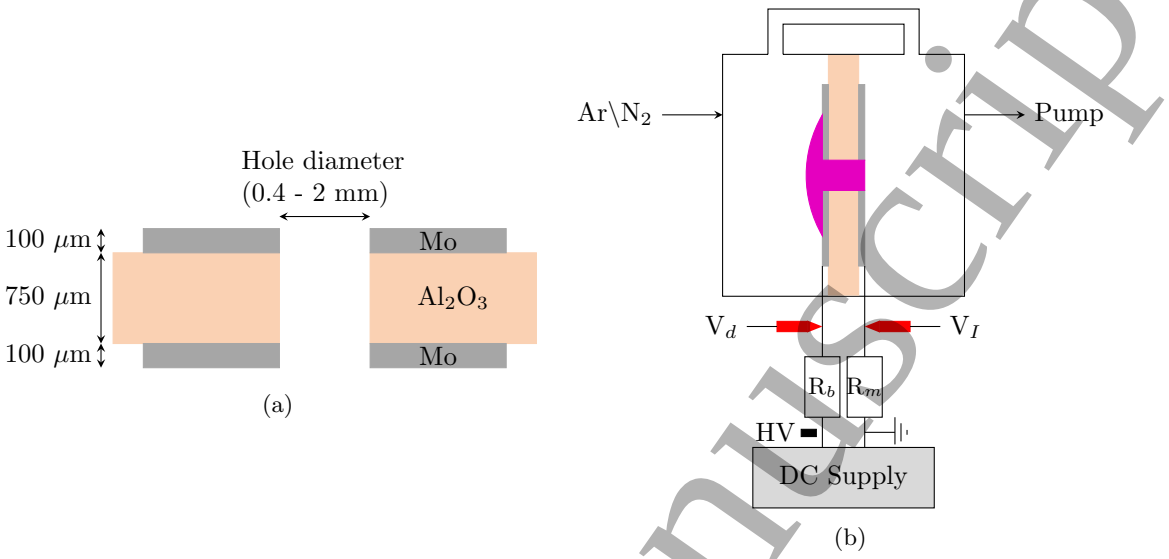

Figure 1: Scheme of (a) the MHCD configuration and (b) the reactor used in the experiments.

2.2 Optical emission spectroscopy : Stark broadening of H_β for electron density determination

The electron density was measured using the Stark broadening of the H_β line at $\lambda_{H_\beta} = 486.135$ nm, which is very sensitive to this type of broadening. To observe the line, 1% of hydrogen gas was added into the gas mixture. It should be noted that, at this low percentage, hydrogen does not affect the discharge behavior, with no modification of its current-voltage characteristic.

A SOPRA Ebert-Fasti monochromator with a 2 m focal length, with a 1200 groves per mm grating, was used. It is backed by a PIMAX3-1024i (Roper Scientific) CCD camera with a 12.8 × 12.8 μm^2 pixel size. A lens with a 30 mm focal length focuses the light emitted by the plasma into the entry slit, 100 μm wide, of the monochromator. The H_β line is recorded at the third diffraction order of the grating, for which the reverse dispersion is 60.7 pm/mm, yielding to 0.7765 pm per pixel. Two filters placed before the monochromator eliminate the light from other diffraction orders of the grating. A low-pass filter, with a 550 nm cutoff wavelength, filters out the emission in the second diffraction order, and a high-pass filter, with a 400 nm cutoff wavelength, suppresses the intense emission of molecular nitrogen second positive system. To avoid the contribution of the light coming from the emission of the cathodic expansion, the monochromator is facing the anodic side. The H_β line profile results from different physical phenomena:
- the apparatus function ($\Delta\lambda_I$) that depends on the width of the slit, the grating, the CCD and the optical aberration. In our case, the instrumental broadening induces a Gaussian profile and $\Delta\lambda_I$ is measured to be of 7.5 pm, using an argon ionic line.
- the Doppler broadening ($\Delta\lambda_D$), due to the thermal agitation of the particles, also induces a Gaussian profile and is calculated as follows [22]:

$$\Delta\lambda_D = \lambda_{H_\beta}\sqrt{8\ln(2)\frac{k_B T_g}{c^2 M}} = 7.16\times10^{-7}\times\lambda_{H_\beta}\sqrt{\frac{T_g}{M}} \quad (1)$$

where T_g is the gas temperature, c the speed of light, M the mass of the hydrogen atom and k_B the Boltzmann constant. With T_g estimated to be of 470 K based on previous measurements on a similar source [23], we obtain $\Delta\lambda_D = 7$ pm.
- the Van der Waals broadening ($\Delta\lambda_{VdW}$) is caused by the collisions with perturbing particles with similar

energy levels as the emitting particle. It induces a Lorentzian profile and is expressed by [24, 25]:

$$\Delta\lambda_{VdW} = 6.8 \times \frac{P_{Ar}}{T_g^{0.7}} + 2.4 \times \frac{P_{N_2}}{T_g^{0.7}} \quad (2)$$

with P_{Ar} and P_{N_2} the partial pressure of Ar and N_2, respectively, in Torr and $\Delta\lambda_{VdW}$ in pm.
- the Stark broadening ($\Delta\lambda_{Stark}$) is due to the interaction between the emitting atoms, ions and free electrons in the plasma, through the electric fields generated by these particles and it is expressed by [22]:

$$\Delta\lambda_{Stark} = 4.7333 \times 200 \left(\frac{n_e}{10^{22}}\right)^{1/1.49} \quad (3)$$

with n_e in m^{-3} and $\Delta\lambda_{Stark}$ in pm. The convolution of the above-described contributions leads to a Voigt profile of width $\Delta\lambda_{exp}$, which is measured experimentally. Figure 2 shows a typical H_β line profile recorded and the associated Voigt fit used to determine $\Delta\lambda_{exp}$.

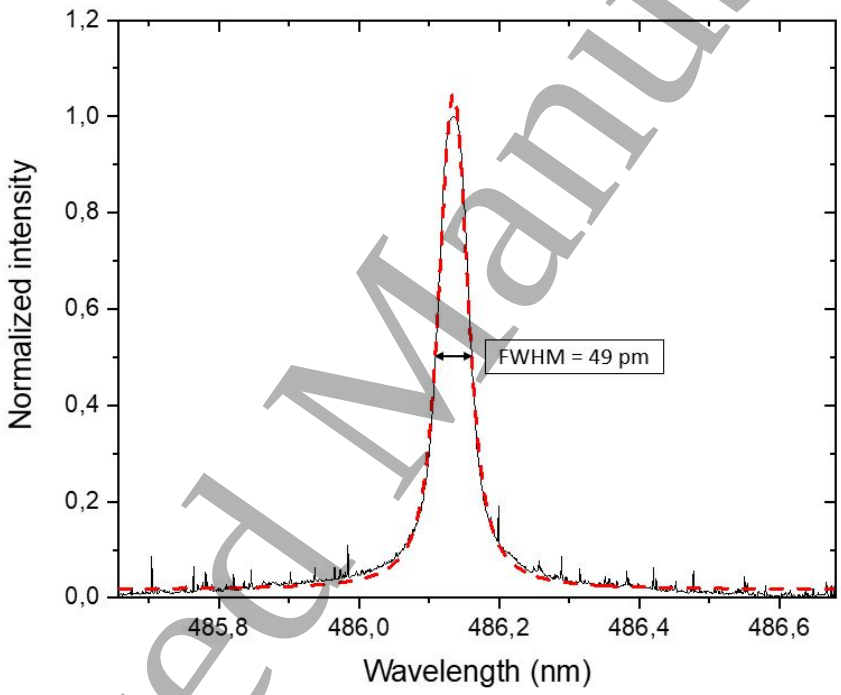

Figure 2: Normalized H_β emission line spectrum (solid black) and corresponding Voigt fit (red dashed). Plasma conditions : Hole diameter = 0.4 mm, P = 50 mbar, 0% N_2, I_d = 1 mA.

Subsequently, the value of the Stark broadening is calculated as follows [26]:

$$\Delta\lambda_{Stark} = \left(\Delta\lambda_{exp}^{1.4} - \Delta\lambda_{DI}^{1.4}\right)^{1/1.4} - \Delta\lambda_{VdW} \text{ with } \Delta\lambda_{DI} = \sqrt{\Delta\lambda_I^2 + \Delta\lambda_D^2} \quad (4)$$

The electron density is then linked to the Stark broadening $\Delta\lambda_{Stark}$ (in pm) through :

$$n_e = 10^{22} \times \left(\frac{\Delta\lambda_{Stark}}{4.7333 \times 200}\right)^{1.49} \text{ m}^{-3} \quad (5)$$

2.3 Fourier Transform Spectrometry Vacuum Ultra-Violet absorption for N atom density determination

The N atom density determination was carried out with the VUV high-resolution Fourier Transform spectrometer (FTS) of the DESIRS (Dichroïsme Et Spectroscopie par Interaction avec le Rayonnement Synchrotron)

beamline at the SOLEIL synchrotron facility. The microplasma reactor was placed in the sample environment chamber of the FTS branch. The usual borosilicate windows were replaced with MgF_2 windows, transparent in the near VUV spectral range. The VUV FTS setup is described in details in [27, 28]. This spectrometer covers the full VUV range down to 40 nm and allows for a very high spectral resolution to be achieved. It records the photo-absorption spectra over the full range, with a resolving power $\frac{\lambda}{\Delta\lambda}$ up to 1×10^6. The N atom density is probed using the transition between the ground state ($2p^3\ ^4S_{3/2}$) and the triplet state ($3s\ ^4P_{1/2,3/2,5/2}$) around 120 nm. The spectrometer yields the full convoluted transmission spectrum $T_C(\sigma')$ (with σ' the wavenumber in cm^{-1}) :

$$T_C(\sigma') = T_0(\sigma')[\Phi_I(\sigma' - \sigma) * T(\sigma)] \tag{6}$$

where $T_0(\sigma')$ is the transmission spectrum without absorbent, $\Phi_I(\sigma' - \sigma)$ the instrumental profile and $T(\sigma)$ the actual absorption spectrum of the sample. In the case of this spectrometer, the instrumental function is a sinc function $\Phi_I(\sigma' - \sigma) = \frac{sin(\pi(\sigma' - \sigma))}{\pi(\sigma' - \sigma)}$, with a Full Width at Half Maximum (FWHM) Δ_I that is proportional to the sampling interval $\delta\sigma'$. In our case, $\Delta_I = 0.53\ cm^{-1}$. The raw data $T_C(\sigma')$ are first normalized to the baseline $T_0(\sigma')$ and deconvoluted from $\Phi_I(\sigma' - \sigma)$ to obtain the transmission spectrum, which, according to Beer-Lambert law, is equal to :

$$T(\sigma) = exp[-Abs(\sigma)] = exp[-k(\sigma).l_{abs}(N)] \tag{7}$$

with $Abs(\sigma)$ the absorbance, $l_{abs}(N)$ the absorption length for the N atoms considered here and $k(\sigma)$ the absorption coefficient. For a single line, between an upper level u and a lower level l, with a central transition wavenumber σ_{ul}, $k(\sigma)$ is given by [29]:

$$k(\sigma) = k_0\Phi(\sigma)(N_l - \frac{g_l}{g_u}N_u) = \frac{g_u}{g_l}\frac{1}{8\pi c\sigma_{ul}^2}A_{ul}\Phi(\sigma)(N_l - \frac{g_l}{g_u}N_u) \tag{8}$$

with g_u and g_l the statistical weights of the upper and lower levels, N_u and N_l the corresponding population densities, c the speed of light, A_{ul} the Einstein coefficient of the transition and $\Phi(\sigma)$ the normalized line profile. Because the gas temperature T_g, estimated to be of 470 K (0.05 eV), is much lower than the energy of the transition (10 eV), we can consider that $N_u \ll N_l$, which thus yields :

$$Abs(\sigma) = \frac{g_u}{g_l}\frac{1}{8\pi c\sigma_{ul}^2}A_{ul}\Phi(\sigma)N_l.l_{abs}(N) \tag{9}$$

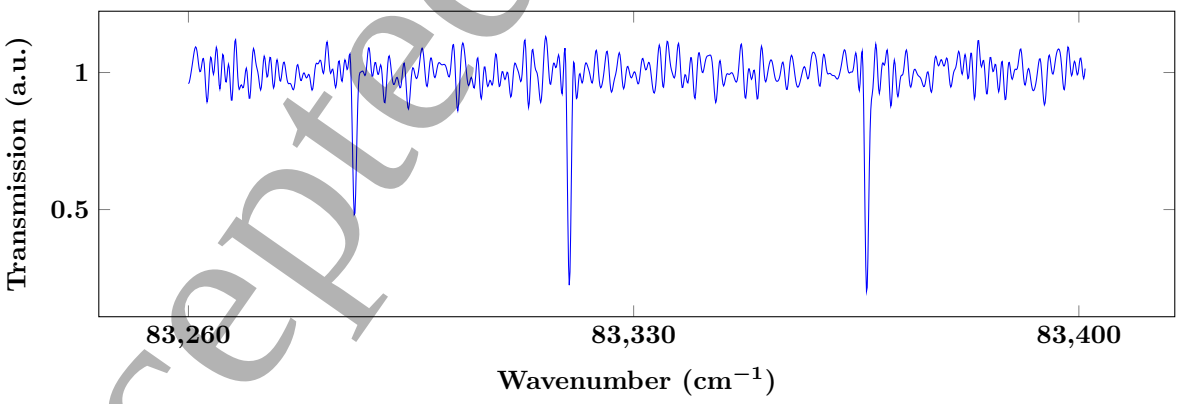

Figure 3: Normalized, non deconvoluted, transmission spectrum of the $N(2p^3\ ^4S_{3/2} \rightarrow 3s\ ^4P_J)$ triplet transition. Plasma conditions : Hole diameter = 1 mm, grazing the anodic side, P = 30 mbar, 20% N_2, I_d = 1 mA.

In the general case, the line profile $\Phi(\sigma)$ is a Voigt profile, i.e. the convolution of a Gaussian and a Lorentzian line profiles. The latter is related to the species lifetime and includes the pressure broadening (estimated to be of 0.01 cm^{-1} in our conditions). The former reflects the thermal motion of the absorbent

atoms, of mass M = 14, with a Doppler FWHM $\Delta\sigma_D = \sigma_{ul}\sqrt{8\ln(2)k_BT_g/Mc^2} = 0.35$ cm^{-1} at $T_g = 470$ K, assumed to be equal to the gas temperature because of the high collision rate.

Figure 3 shows the normalized, non deconvoluted transmission spectrum of the three transitions from the ground state of nitrogen ($2p^3\ ^4S_{3/2}$) to the triplet state ($3s\ ^4P_{1/2,3/2,5/2}$), for the case of a 1 mm diameter hole, a gas mixture of 80% Ar and 20% N_2, a pressure of 30 mbar and a discharge current of 1 mA. Each line is individually fitted with a convolution of a sinc function and a Voigt profile, with fixed values for the instrumental function FWHM Δ_I and the Doppler broadening $\Delta\sigma_D$. In all of our experimental conditions, grazing the cathodic side, with percentages of N_2 as low as 1%, we faced a saturation of the absorption line. The line fitting was done only on the non-saturated wings of the Voigt profile, allowing us to still obtain a measurement but with less precision. Fitting each line individually grants us with a mean value and a standard error. The error on the column density $N_l.l_{abs}(N)$, which is due to the signal-to-noise ratio obtained in each condition, can reach up to 20%, depending on the experimental conditions. This measurement is not affected by the reproducibility of the discharge since only one set of measurements has been performed, due to time constraints.

2.4 Tunable diode laser absorption spectroscopy for Ar* density determination

The determination of the Ar* density was carried out with an experimental setup based on that previously reported in [30] and illustrated in figure 4. The transition probed is the one at 811.531 nm between the metastable states ($4s\ ^3P_2$) and ($4p\ ^3D_3$) (transition referred as ($1s_5 \rightarrow 2p_9$) in Paschen's notation), using the commercial diode laser Toptica DL 100 DFB-L. The wavelength of the laser is adjusted between 811.501 and 811.561 nm to scan the entire line profile. This is done by modifying the operating current of the laser.

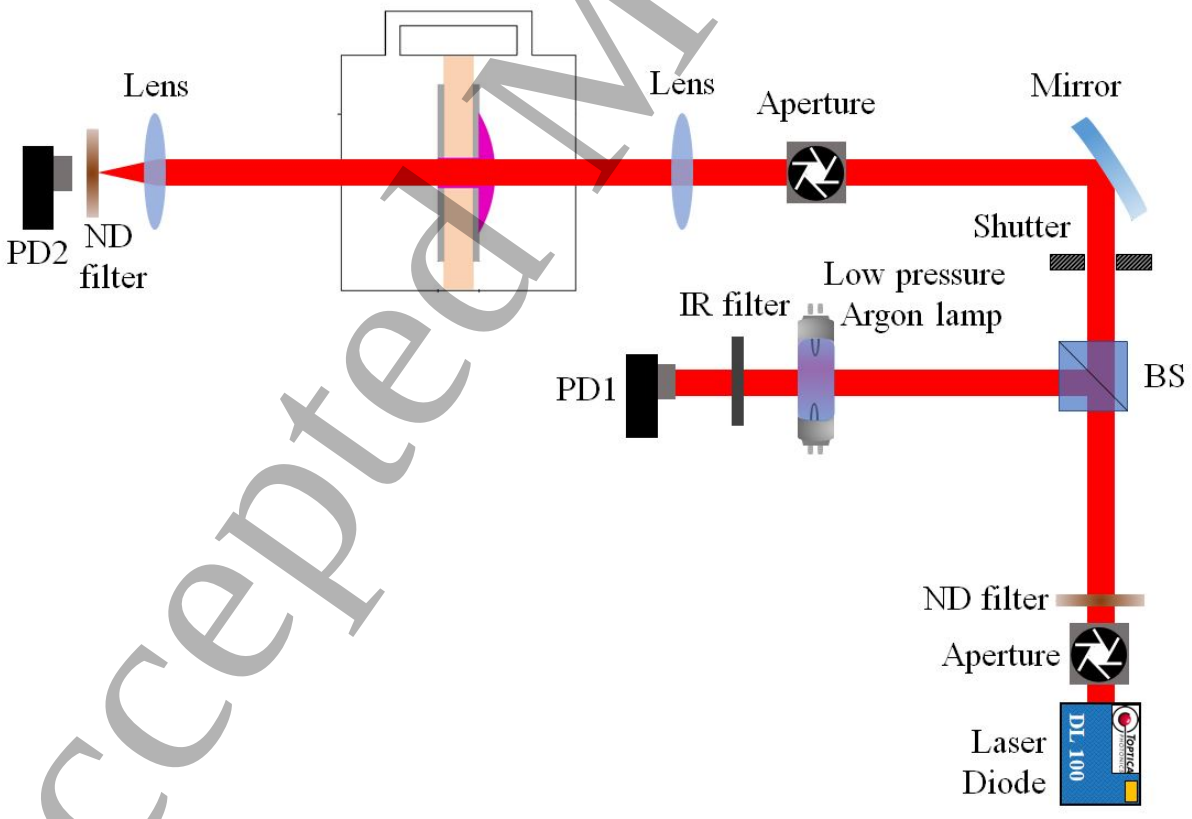

Figure 4: Experimental setup used for the determination of the Ar* density. PD = PhotoDiode, ND filter = Neutral Density filter, IR filter = Infra-Red filter, BS = Beam Splitter.

The laser beam passes through an aperture and a neutral optical density (ND filter in figure 4) to sufficiently attenuate its intensity and avoid any saturation of the optical transition. The beam is then divided in two parts with a beam spliter (BS) : the first part passes through a low-pressure argon lamp used as a reference for the determination of the central wavelength of the transition, and the second part goes through the microplasma source. The beam probing the plasma is shaped by the aperture put before the reactor. Hence, the laser spot probing the medium is circular with a 1 mm diameter. After passing through the plasma, the laser beam is focused with a lens into a photodiode (PD2).
To record the absorbance of the plasma as a function of the laser wavelength, four signals are recorded for each plasma condition : the transmission T (laser ON, plasma ON), the plasma emission P (laser OFF, plasma ON), the laser emission L (laser ON, plasma OFF) and the background noise B (laser OFF, plasma OFF). The absorbance (Abs) is then calculated as follows:

$$Abs(\lambda) = -\frac{T(\lambda) - P(\lambda)}{L(\lambda) - B(\lambda)} \tag{10}$$

As seen previously in section 2.3, the absorbance is related to the population density of the lower level through equation (9). However, instead of fitting the line profile, we directly used the integral of the absorbance :

$$N_l = \frac{g_l}{g_u}\frac{8\pi}{\lambda_{ul}^2}\frac{1}{A_{ul} l_{abs}(Ar^*)}\int Abs(\nu)d\nu \tag{11}$$

with ν the frequency, λ_{ul} the central wavelength of the line and given that the integral of the normalized line profile $\int \Phi(\nu)d\nu = 1$. This allows us to make no assumption on the shape of the line profile. Each experience was repeated at least three times, yielding a standard deviation on the column density $N_l.l_{abs}(Ar^*)$ between 20 and 50%, depending on the experimental conditions. The error increases with the percentage of N_2 in the discharge since the density of Ar* decreases and, consequently, the signal-to-noise ratio decreases as well. The reproducibility of the discharge from day to day is another source of error for this diagnostic.

2.5 0D model

The experimental results obtained have been compared to those given by a 0D model of the discharge, yielding the volume averaged densities of species (including electrons), reaction rates and electron temperature. The model is based on a previous one [31, 32], upgraded with an adapted chemistry to study the Ar/N_2 gas mixture. 14 species are taken into consideration : ground-state argon atoms Ar, argon positive ions Ar^+, argon molecular ions Ar_2^+, metastable argon atoms Ar^m, resonant argon atoms Ar^r, excited argon atoms in the 4p state Ar^{4p}, ground-state molecular nitrogen N_2, electronically excited N_2 molecules ($N_2(A)(A^3\Sigma_u^+)$, $N_2(B)(B^3\Pi_g)$ and $N_2(C)(C^3\Pi_u)$), nitrogen atoms N, the positive nitrogen ions N_2^+ and N_4^+, and the electrons e. The Ar^r includes the two resonant states $^1P_1$ and $^3P_1$, while the Ar^m state includes both the $^3P_2$ ($1s_5$ in Paschen's notation) and the $^3P_0$ ($1s_3$ in Paschen's notation). We bring to the reader's attention that our absorption spectroscopy measurements relate to the density of metastable argon in the $^3P_2$ ($1s_5$) only. In the literature, the density ratio between the $1s_5$ and $1s_3$ states have been measured and found between 6.25 and 8.9 [33,34], which gives an idea of the expected discrepancy between the experimental and the model results. On the basis of previous works [21, 23, 31, 35–44] in similar gas mixtures, we are considering 69 reactions in the plasma volume, gathered in table 1.

n	Reaction	Reaction rate	Reference
Electron impact ionization			
R1	$e + Ar \rightarrow Ar^+ + e + e$	$2.34 \times 10^{-14} \times T_e^{0.59} \times \exp(-17.44/T_e)$	[35]
R2	$e + Ar^m \rightarrow Ar^+ + e + e$	$6.8 \times 10^{-15} \times T_e^{0.67} \times \exp(-4.2/T_e)$	[35]
R3	$e + Ar^{4p} \rightarrow Ar^+ + e + e$	$1.8 \times 10^{-13} \times T_e^{0.61} \times \exp(-2.61/T_e)$	[35]
R4	$e + N_2 \rightarrow N_2^+ + e + e$	$1.34 \times 10^{-14} \times T_e^{0.7224} \times \exp(-22.38/T_e)$	[36]
Electron impact excitation and de-excitation			
R5	$e + Ar \rightarrow Ar^m + e$	$5 \times 10^{-15} \times \exp(-12.64/T_e) + 1.4 \times 10^{-15} \times \exp(-12.42/T_e)$	[35]

Continues on next page...

n	Reaction	Reaction rate	Reference
R6	$e + Ar \rightarrow Ar^r + e$	$1.9 \times 10^{-15} \times \exp(-12.6/T_e) + 2.7 \times 10^{-16} \times \exp(-12.14/T_e)$	[35]
R7	$e + Ar \rightarrow Ar^{4p} + e$	$2.1 \times 10^{-14} \times \exp(-13.13/T_e)$	[35]
R8	$e + Ar^m \rightarrow Ar + e$	$4.3 \times 10^{-16} \times T_e^{0.74}$	[35]
R9	$e + Ar^m \rightarrow Ar^r + e$	3.7×10^{-13}	[35]
R10	$e + Ar^m \rightarrow Ar^{4p} + e$	$8.9 \times 10^{-13} \times T_e^{0.51} \times \exp(-1.59/T_e)$	[35]
R11	$e + Ar^r \rightarrow Ar + e$	$4.3 \times 10^{-16} \times T_e^{0.74}$	[35]
R12	$e + Ar^r \rightarrow Ar^m + e$	9.1×10^{-13}	[35]
R13	$e + Ar^r \rightarrow Ar^{4p} + e$	$8.9 \times 10^{-13} \times T_e^{0.51} \times \exp(-1.59/T_e)$	[35]
R14	$e + Ar^{4p} \rightarrow Ar^r + e$	$3 \times 10^{-13} \times T_e^{0.51}$	[35]
R15	$e + Ar^{4p} \rightarrow Ar^m + e$	$3 \times 10^{-13} \times T_e^{0.51}$	[35]
R16	$e + Ar^{4p} \rightarrow Ar + e$	$3.9 \times 10^{-16} \times T_e^{0.71}$	[35]
R17	$e + Ar^+ \rightarrow Ar^m$	$5.95 \times 10^{-17} \times T_e^{0.5}$	[35]
R18	$e + e + Ar^+ \rightarrow Ar^m + e$	$5.6 \times 10^{-39} \times T_e^{-4.5}$	[23]
R19	$e + Ar_2^+ \rightarrow Ar^m + Ar$	$5.4 \times 10^{-14} \times T_e^{-2/3}$	[31]
R20	$e + e + N_2^+ \rightarrow N_2 + e$	$5.651 \times 10^{-39} \times T_e(K)^{-0.8}$	[37]
R21	$e + N_2 \rightarrow N + N + e$	$1.959 \times 10^{-12} \times T_e(K)^{-0.7} \times \exp(-1.132 \times 10^5/T_e(K))$	[37]
R22	$e + N_2^+ \rightarrow N_2$	$4.8 \times 10^{-13} \times T_e(K)^{-0.5}$	[38]
Ion molecule reactions			
R23	$Ar^+ + Ar + Ar \rightarrow Ar_2^+ + Ar$	2.5×10^{-43}	[23]
Neutral reactions : Penning ionization			
R24	$Ar^m + Ar^r \rightarrow Ar + Ar^+ + e$	2.1×10^{-15}	[35]
R25	$Ar^{4p} + Ar^{4p} \rightarrow Ar + Ar^+ + e$	5×10^{-16}	[35]
R26	$Ar^m + Ar^m \rightarrow Ar + Ar^+ + e$	6.4×10^{-16}	[35]
Neutral reactions			
R27	$Ar + Ar^m \rightarrow Ar + Ar$	2.1×10^{-21}	[35]
R28	$Ar^m + N_2 \rightarrow N + N + Ar$	3.6×10^{-17}	[21]
R29	$Ar^r + N_2 \rightarrow N + N + Ar$	3.6×10^{-17}	[21]
Dissociative recombination			
R30	$e + e + N_4^+ \rightarrow N_2 + N_2 + e$	$5.651 \times 10^{-39} \times T_e(K)^{-0.8}$	[37]
R31	$e + N_2^+ \rightarrow N + N$	$4.8 \times 10^{-13} \times (T_e(K)/300)^{0.5}$	[21]
R32	$e + N_4^+ \rightarrow N_2 + N_2$	$2 \times 10^{-12} \times (T_e(K)/300)^{0.5}$	[21]
Ion neutral reactions			
R33	$Ar^+ + N_2 \rightarrow N_2^+ + Ar$	4.45×10^{-16}	[21]
R34	$Ar + N_2^+ \rightarrow N_2 + Ar^+$	2.81×10^{-16}	[21]
R35	$N_2^+ + N_2 + Ar \rightarrow N_4^+ + Ar$	$8.9 \times 10^{-42} \times (Tg/300)^{-1.54}$	[36]
R36	$N_4^+ + N_2 \rightarrow N_2^+ + N_2 + N_2$	$2.1 \times 10^{-22} \times (Tg/121)^{-1.54}$	[21]
R37	$N_2^+ + N_2 + N_2 \rightarrow N_4^+ + N_2$	$6.8 \times 10^{-41} \times (Tg/300)^{1.64}$	[21]
R38	$N_4^+ + Ar \rightarrow Ar^+ + N_2 + N_2$	1×10^{-17}	[21]
Radiation			
R39	$Ar^r \rightarrow Ar$	1.77×10^6	[39]
R40	$Ar^{4p} \rightarrow Ar^m$	1.5×10^7	[35]
R41	$Ar^{4p} \rightarrow Ar^r$	1.5×10^7	[35]

Continues on next page...

n	Reaction	Reaction rate	Reference
Electronically excited states of N_2 reactions			
R42	$N + N + N_2 \rightarrow N_2(A) + N_2$	1.7×10^{-45}	[40]
R43	$N + N + N \rightarrow N_2(A) + N$	1×10^{-44}	[40]
R44	$N + N + N_2 \rightarrow N_2(B) + N_2$	2.4×10^{-45}	[40]
R45	$N + N + N \rightarrow N_2(B) + N$	1.4×10^{-44}	[40]
R46	$N_2(A) + N \rightarrow N_2 + N$	2×10^{-18}	[40]
R47	$N_2(A) + N_2 \rightarrow N_2 + N_2$	3×10^{-22}	[40]
R48	$N_2(A) + N_2(A) \rightarrow N_2 + N_2(C)$	1.5×10^{-16}	[40]
R49	$N_2(A) + N_2(A) \rightarrow N_2 + N_2(B)$	3×10^{-16}	[40]
R50	$N_2(B) + N_2 \rightarrow N_2 + N_2$	3×10^{-17}	[40]
R51	$N_2(B) + N_2 \rightarrow N_2(A) + N_2$	5×10^{-17}	[41]
R52	$N_2(B) \rightarrow N_2(A)$	1.5×10^{5}	[41]
R53	$N_2(C) \rightarrow N_2(B)$	3×10^{7}	[41]
R54	$N_2(C) + N_2 \rightarrow N_2(B) + N_2$	3×10^{-17}	[41]
R55	$N_2(C) + N_2 \rightarrow N_2(A) + N_2$	1.1×10^{-17}	[41]
R56	$N_2 + Ar^m \rightarrow N_2(C) + Ar$	3.6×10^{-17}	[42]
R57	$N_2(A) + N_2(A) \rightarrow N_4^+ + e$	1×10^{-19}	[43]
R58	$N_2(A) + N_2(A) \rightarrow N_2 + N + N$	3×10^{-17}	[43]
R59	$N_2(A) \rightarrow N_2$	5×10^{-1}	[43]
R60	$N_2(B) + Ar \rightarrow N_2(A) + Ar$	3×10^{-19}	[43]
R61	$N_2 + Ar^r \rightarrow N_2(C) + Ar$	3.6×10^{-17}	[43]
R62	$N_2(C) + Ar \rightarrow N_2(B) + Ar$	8×10^{-19}	[44]
R63	$N_2(A) + N_2(A) \rightarrow N_2(A) + N_2(B)$	4×10^{-17}	[44]
R64	$N_2(A) + N_2(A) \rightarrow N_2(A) + N_2(C)$	1.5×10^{-17}	[44]
R65	$N_2(C) + e \rightarrow N_2(B) + e$	1.5×10^{-17}	[44]
R66	$N_2(B) + e \rightarrow N_2(A) + e$	2×10^{-18}	[44]
R67	$N_2(A) + e \rightarrow N_2 + e$	2×10^{-18}	[44]
R68	$N_2 + e \rightarrow N_2(B) + e$	3×10^{-16}	[44]
R69	$N_2 + e \rightarrow N_2(C) + e$	3×10^{-16}	[44]

Table 1: Reactions and corresponding reaction rates used in the 0D model. T_e is the electronic temperature in eV, T_e(K) the electronic temperature in K. The gas temperature T_g is expressed in K as well. The reaction rates are in $m^3.s^{-1}$ for two-body reactions, in $m^6.s^{-1}$ for three-body reactions and in s^{-1} for radiative decay.

In addition to the reactions listed in table 1, the ions and excited neutral species are also lost at the surfaces. For neutral species x, the diffusion flux rate to the surface is given by :

$$K_x = \left(\frac{\Lambda^2}{D_x} + \frac{2V(2-\gamma_x)}{\gamma_x S v_x} \right)^{-1} \tag{12}$$

with $\Lambda = [(\pi/L)^2 + (2.405/R)^2]^{-1/2}$ the effective diffusion length, V/S the volume to surface ratio of the discharge, γ_x the recombination coefficient and $v_x = (8k_B T_g/\pi m_x)^{1/2}$ the neutral atom mean velocity, where m_x is the neutral atom mass. D_x is the diffusion coefficient and it is inversely proportional to the pressure, such that at pressure P, temperature T_g, $D_x(P, T_g) = D_x$(atm. pressure, 300 K)×1013/P×$(T_g/300)^{1.5}$. Ion

losses at the surface are described with the ion flux for a positive ion i expressed as follows:

$$\Gamma_i = h_{Ri} u_{Bi} n_i \tag{13}$$

with $u_{Bi} = (\mathrm{eT}_e/\mathrm{m}_i)^{0.5}$ the Bohm velocity, where e is the elementary charge, T_e the electronic temperature and m_i the mass of ion i. h_{Ri} is the edge-to-center density ratio calculated by :

$$h_{Ri} = \frac{\chi_{01} J_1(\chi_{01})}{R u_{Bi}} D_{ai} = \frac{\chi_{01} J_1(\chi_{01})}{R u_{Bi}} \frac{k_B T_i}{m_i \nu_i} \left(1 + \frac{T_e}{T_i}\right) \tag{14}$$

where $\chi_{01} = 2.405$ is the first zero of the Bessel function J_0, $J_1(\chi_{01}) = 0.52$, D_{ai} the ambipolar diffusion coefficient, T_i the ion temperature equal to the gas temperature and ν_i the collision frequency. We use $\nu_i = n_g \sigma_i \bar{\nu_i}$ with $\sigma_i = 10^{-18}$ m^2 and $\bar{\nu_i} = (8 k_B T_i/\pi m_i)^{1/2}$. All of the surface reactions considered and relevant parameters can be found in table 2. For every condition in the model, we use $\mathrm{T}_g = 470$ K, based on previous work [23].

n	Reaction	D ($\mathrm{m}^2.\mathrm{s}^{-1}$)	γ	Reference
R70	$Ar^+ \rightarrow Ar$			[45]
R71	$Ar_2^+ \rightarrow Ar + Ar$			[45]
R72	$N_2^+ \rightarrow N_2$			[45]
R73	$N_4^+ \rightarrow N_2 + N_2$			[45]
R74	$N \rightarrow \frac{1}{2}N_2$	9.41×10^{-5}	0.1	[46]
R75	$N_2(A) \rightarrow N_2$	5.47×10^{-5}	1	[43]
R76	$N_2(B) \rightarrow N_2$	5.47×10^{-5}	1	[43]
R77	$N_2(C) \rightarrow N_2$	5.47×10^{-5}	1	[43]
R78	$Ar^m \rightarrow Ar$	1.09×10^{-5}	1	[45]
R79	$Ar^r \rightarrow Ar$	1.09×10^{-5}	1	[45]
R80	$Ar^{4p} \rightarrow Ar$	1.09×10^{-5}	1	[45]

Table 2: Surface reactions and corresponding diffusion coefficients and reaction probabilities used in the 0D model.

The electron energy balance equation is:

$$\frac{d}{dt}\left(\frac{3}{2} n_e k_B T_e\right) = P_{\mathrm{abs}} - P_{\mathrm{loss}} \tag{15}$$

with P_{abs} the absorbed power by the electrons and P_{loss} the dissipated power by the electrons.

The expression of the absorbed power by the electrons is [39]:

$$P_{\mathrm{abs}} = \frac{A}{S_C}(1-\kappa) V_d \times I_d \tag{16}$$

with A the inner surface of the cathodic region ($A = 2\pi R L_{\mathrm{cath}}$ with R the radius of the hole and L_{cath} the cathode thickness), S_C the surface through which the discharge current flows and κ the fraction of the power dissipated by ions accelerated in the cathode sheath. The ratio A/S_C and κ are taken equal to 0.5 and 0.75, respectively, in our conditions.

Concerning the dissipated power by the electrons, we have used the formulation of the collisional energy loss proposed by Thorsteinsson *et al.* [46], which includes the losses related to vibrational levels of nitrogen molecules and higher electronic levels of nitrogen atoms and molecules. The evolution of the collisional loss as a function of the electron temperature given in [46,47] has been calculated assuming a Maxwellian electron energy distribution.

2.6 Probed areas and absorption lengths

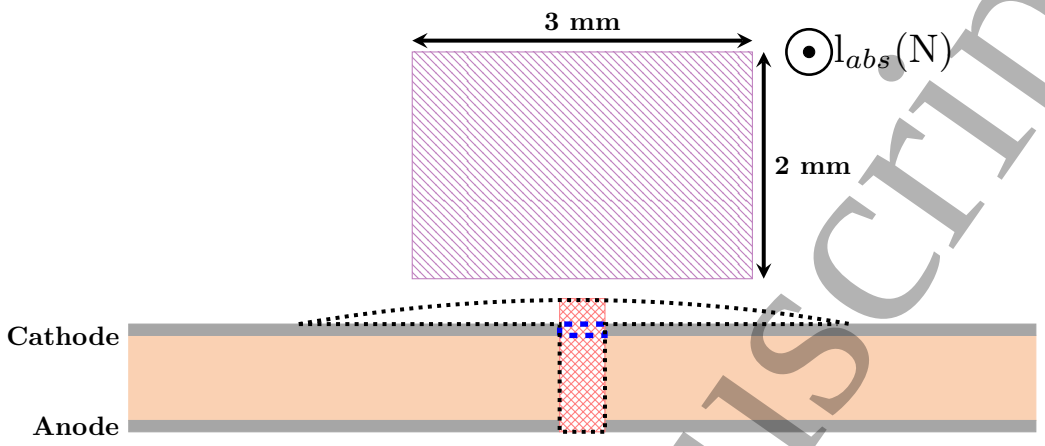

Figure 5: Scheme of the areas probed by the different diagnostics, at scale, for a 0.4 mm diameter hole. The dotted black line shows the limits of the visible plasma. The blue dashed line shows the volume considered in the model. The red crosshatched area is the one over which the average electron density is measured, while the purple hatched area is the one probed by the VUV FTS (N atom density).

In this section, we summarize the information gathered about the discharge through the different diagnostics and the 0D model. Figure 5 shows a scheme of the diagnostics performed, with the visible plasma delimited by the black dashed line. The 0D model computes the volume-averaged density of species over the cathodic area, delimited with the blue dashed line (in volume, it is a cylinder with the same diameter as the hole and the height of the cathode). This is the plasma region where most of the electric power is deposited [31] and, thus, where the densities are expected to be the highest.

The TDLAS measurements give the Ar* column density along the axis of the hole. Ar metastables are mainly created in the cathodic region (see blue dashed line in figure 5) by excitation by the energetic electrons, which are localized in this region, and are lost at the surface. Their concentration is, thus, localized in this region and, therefore, the absorption length has been estimated to be comparable to the hole radius (for example, l_{abs}(Ar*)=200 μm for a hole diameter of 400 μm). In what regards the OES, the light collected comes from the red crosshatched area. Hence, the electron density measured is the average density in this area.

The purple hatched rectangle shows the area over which the VUV FTS diagnostic probes for the N atom density. The VUV beam spot is a 2 by 3 mm rectangle, represented as plane in figure 5. The effective length of the volume probed by the laser spot is l_{abs}(N), and has been estimated using a simple diffusion model. Indeed, in the Ar/N_2 gas mixture, the N atoms losses in the volume can only occur through three-body collisions with N_2 molecules and Ar atoms with reaction coefficients of, respectively, $k_{N_2} = 8.27 \times 10^{-34} \times \exp(500/T_g(K))$ $cm^6 s^{-1}$ and $k_{Ar} = 0.05 \times k_{N_2}$ [21]. In our conditions, this results in a lifetime of about a minute and can be neglected. We, thus, resolve the diffusion equation, with no loss in the volume. The considered configuration is illustrated in figure 6a where half of the reactor is represented. The total radius of the reactor is 50 mm (L/2). The N atoms diffuse in the three dimensions, from the sphere of radius R_0 (i.e. the radius of the hole) where the density is assumed uniform and equal to n_0. The diffusion equation in spherical coordinates, in the stationary regime, is then written as:

$$\Gamma(r) = -D\frac{\partial n(r)}{\partial r} \tag{17}$$

where Γ and n are the flux and the density of N atoms, respectively, and D is the diffusion coefficient (given in table 2).
The conservation equation for N atoms, when the recombination in the volume is neglected, can be expressed as follows:

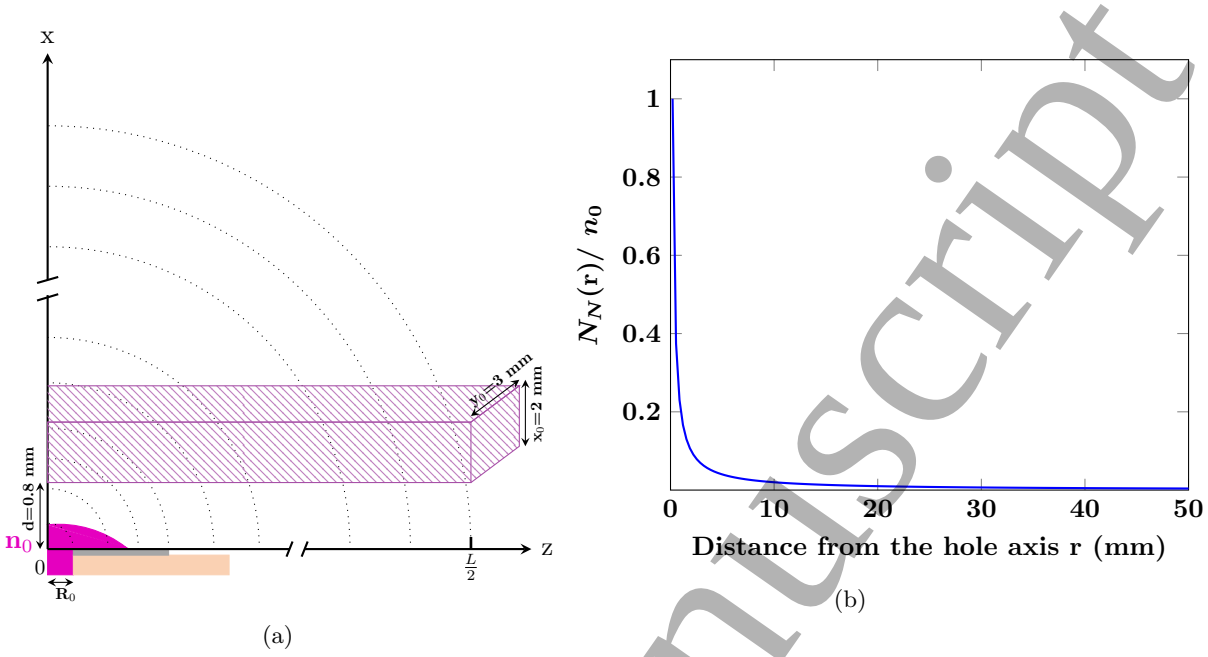

Figure 6: (a) Schema of the diffusion of N atoms in the reactor. Half the cathodic chamber is represented. The hatched area represents the path of the VUV FTS laser beam. Geometric parameters used for the evaluation of $l_{abs}(N)$ are represented. (b) N atoms density as a function of the distance from the hole axis, as calculated by the spherical diffusion model.

$$div\vec{\Gamma} = 0 \tag{18}$$

Normalizing by $\Gamma_0 = \frac{n_0 D}{R_0}$ the flux at r = R_0 and solving the equation yields the following expression for the N atoms density as a function of the radial position r:

$$n(r) = \frac{R_0 n_0}{r} \tag{19}$$

which gives in cartesian coordinates:

$$n(x,y,z) = \frac{R_0 n_0}{\sqrt{x^2+y^2+z^2}} \tag{20}$$

The profile of the N atoms density found is plotted in figure 6b. In order to determine the effective absorption length l_{abs}(N), this density profile has to be integrated on the volume probed by the laser. For a given wavelength σ, the absorbance signal gathered by the FTS technique is :

$$\begin{aligned} Abs(\sigma) &= \frac{k(\sigma)}{x_0 y_0} \int_d^{d+x_0} \int_{-\frac{y_0}{2}}^{\frac{y_0}{2}} \int_{-\frac{L}{2}}^{\frac{L}{2}} n(x,y,z)dxdydz \\ &= k(\sigma) n_0 \frac{R_0}{x_0 y_0} \int_d^{d+x_0} \int_{-\frac{y_0}{2}}^{\frac{y_0}{2}} \int_{-\frac{L}{2}}^{\frac{L}{2}} \frac{1}{\sqrt{x^2+y^2+z^2}} dxdydz \\ &= k(\sigma) n_0 l_{\text{abs}}(N) \end{aligned} \tag{21}$$

where x_0 = 2 mm, y_0 = 3 mm and L = 50 mm are the dimensions of the volume probed by the laser beam and d the distance between the edge of the hole and the laser beam, as defined in figure 6a. The effective absorption length l_{abs}(N) is then obtained by integrating numerically the triple integral and we get the following results for the three different hole radius considered in this study:

$$\begin{aligned} l_{\text{abs}}(N) &= 1.58 \text{ mm for } R_0 = 0.2 \text{ mm} \\ &= 3.95 \text{ mm for } R_0 = 0.5 \text{ mm} \\ &= 7.90 \text{ mm for } R_0 = 1 \text{ mm} \end{aligned} \quad (22)$$

Using these values in equation 9, it yields n_0, the N atoms density at the frontier with the visible plasma, close to the area considered in the model.

3 Results and discussion

As a reminder, in this study, the discharge current was maintained at 1 mA for every condition and the gas temperature was assumed to be at $T_g = 470$ K. The range of parameters covered for the measurement of the density of Ar*, e and N may differ due to the time and diagnostic constraints. The input data of the model (V_d, I_d, P, $\%N_2$, Hole diameter) are those gathered experimentally.

3.1 Effect of the hole diameter

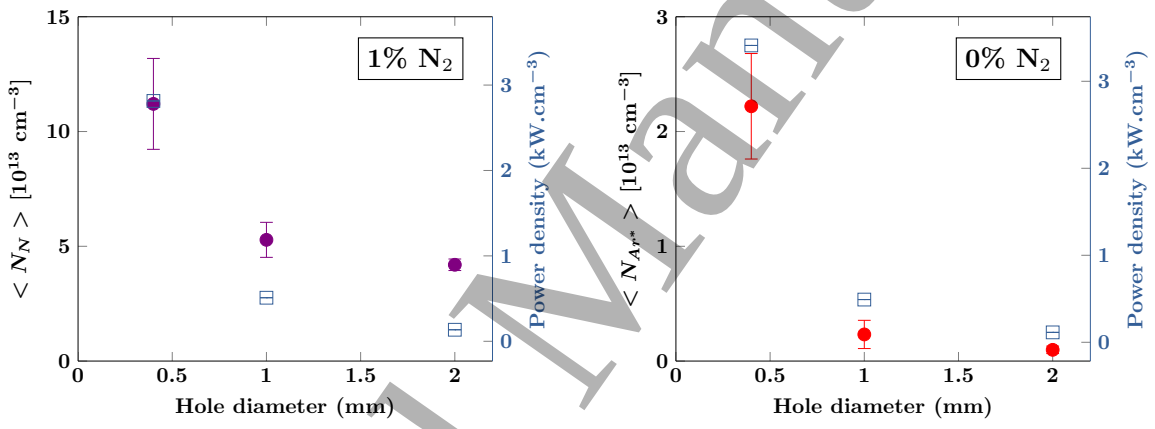

(a) (b)

Figure 7: Experimental densities of (a) N atoms (purples circles) and (b) Ar* (red circles), and associated power densities in the hole (blue squares) for three hole diameters. P = 50 mbar, I_d = 1 mA.

The first parameter studied was the hole diameter. Figure 7 shows the evolution of the N atom and Ar* densities, as a function of the hole diameter. The densities show a clear decrease when the hole diameter increases. At 0% N_2, the corresponding discharge voltage V_d remains constant independently of the hole diameter, around 250 V. At 1% N_2, however, the discharge voltage increases with the hole diameter, from 700 V at 0.4 mm to 800 V at 2 mm, following the Paschen curve, and, thus, showing that the chemistry of the plasma changes drastically, even with very few N_2 admixed, as it is well documented in the literature [21, 33, 48]. The discharge power ($I_d \times V_d$) increases thus slightly with the hole diameter. However, the corresponding power density (($I_d \times V_d$)/V, V being the volume of the hole) inside the holes, plotted in figure 7 in blue squares, decreases. This leads to a less energetic plasma and lower excited species densities, explaining the trends observed in figure 7 for Ar* and N atoms. In this study, the electron density has not been measured as a function of the hole diameter. Nonetheless, the decrease of the electron density with the increase of the hole diameter has been previously reported. For example, in helium in [49] and [50], where, under the same conditions, the electron density becomes 1.5 times lower when the diameter increases from 0.3 to 1 mm. To optimize the dissociation of N_2 and the production of N atoms, a smaller hole diameter is thus desired, but this effect is limited by the recombination at the wall and by the constraints of the application (for instance, the gas flux through the hole for deposition processes).

3.2 Effect of the gas pressure

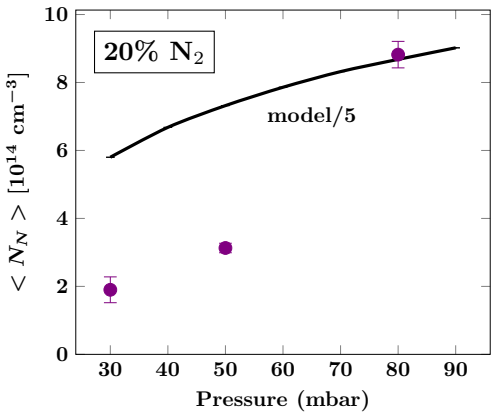

(a)

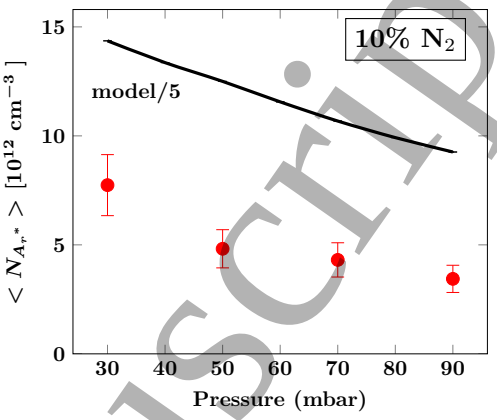

(b)

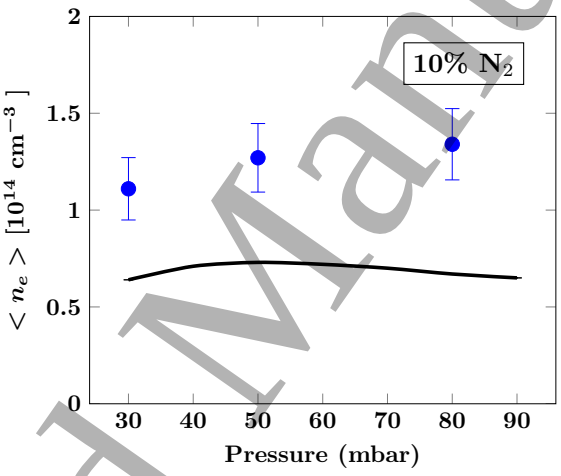

(c)

Figure 8: Experimental densities of (a) N atoms, (b) Ar* and (c) e as a function of the gas pressure. The corresponding calculated densities are also plotted (solid lines). Hole diameter = 0.4 mm, I_d = 1 mA.

Figure 8 shows the evolution of the N atom density, the Ar* density and the electron density as a function of the gas pressure in the reactor. In figure 8a, one can observe that the density of N atoms increases with the pressure both in the model (solid black line) and in the experiments (purple dots). There is a reasonable agreement between the experiments and the model but this latter overestimates the N atoms density. The density of any species is expected to increase linearly with the pressure, without a modification of the production and loss scheme. However, figure 8b seems to show that the production and loss scheme changes. Indeed, in figure 8b, we observe a decrease of the density of Ar* with the pressure predicted both by the experiments and the model. Figure 8c shows that the measured electron density increases slightly on the considered pressure range. The model does not deviate too much, with a small increase between 30 and 50 mbar, and a slight decrease between 50 and 80 mbar. Therefore, it seems that, at a higher pressure, the production of N atoms increases, consuming possibly Ar* through the reaction $Ar^m + N_2 \rightarrow N + N + Ar$ (R28), while the gain-loss balance of electrons remains similar.

To better understand these trends, we plotted in figure 9 the calculated relative contribution of the non-negligible processes of production of N atoms and loss of Ar^m at 10% N_2. In figure 9a, we can see that the model predicts that reaction R28 is the main production path of N atoms over the pressure range considered. We can observe that the contributions of the electron processes $e + N_2 \rightarrow N + N + e$ (R21) and $e + N_2^+ \rightarrow$

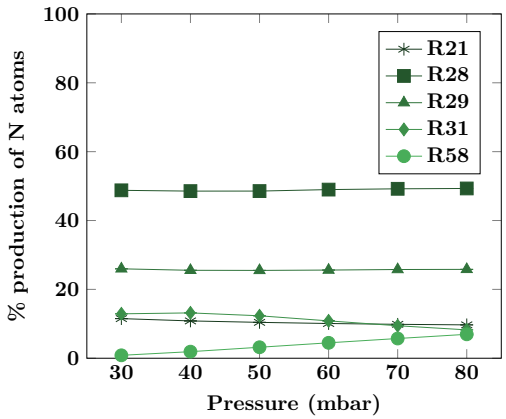

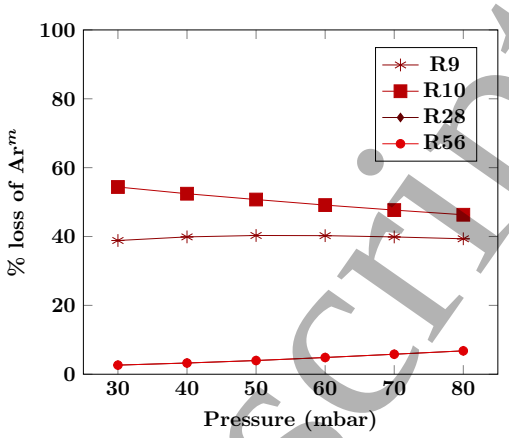

Figure 9: Calculated relative contributions of the non-negligible processes of (a) N atom production and (b) Ar^m loss, as a function of the gas pressure. Hole diameter = 0.4 mm, I_d = 1 mA, 10% N_2.

.

N + N (R31) are almost constant in the considered pressure range, which is consistent with the evolution of the electron density predicted by the model in figure 8c. On the other hand, the contribution of $N_2(A)$ + $N_2(A) \rightarrow N_2 + N + N$ (R58) is increasing with the pressure, explaining partially the increase of the N atoms density in figure 8a. In figure 9b, we can see that the model predicts a decrease with the pressure of the contribution to the loss of Ar^m of the electron-impact reaction $e + Ar^m \rightarrow Ar^{4p} + e$ (R10) and a constant contribution of $e + Ar^m \rightarrow Ar^r + e$ (R9), while the contributions of R28 and R56 (which are superimposed) increase. It is, however, worth noting that R10 is not an effective loss process of Ar^m since the produced Ar^{4p} rapidly decay back to the Ar^m state through reaction R40.

To obtain a maximum N atom production, one should increase the gas pressure in the reactor. However, this will also lead to an increased breakdown voltage and thus an appropriate power supply is needed to provide higher electric power.

3.3 Effect of the gas mixture

Figure 10 represents the densities of N atoms, Ar* and e as a function of the percentage of N_2 into the gas mixture. When adding N_2 in the gas mixture, the density of N atoms greatly increases (figure 10a), but not linearly as it would be expected from the effect of the added N_2 only. The 0D model depicts a different trend, with a maximum of density reached around 10% of N_2. At the same time, the density of Ar* decreases (figure 10b), but, again, not linearly as it would be expected from the removal of Ar in the gas mixture. This suggests a modification of the dominating production paths of N atoms. In figure 10c, we can see that the measured electron density remains almost constant between 0 and 20% of N_2, and then drops by one order of magnitude between 20 and 40% of N_2. Beyond this percentage, we reach the detection limit of the method. The experimental decrease of the electron density is well captured by the model but not the plateau between 0 and 20% of N_2.

To better understand how the production scheme of N atoms is modified by the content of N_2 in the gas mixture, figure 11 shows the calculated relative contributions of the non-negligible production processes of N atoms and loss processes of Ar^m. In figure 11a, we can see that, at very low N_2 percentages, the dissociative electron-ion recombination with N_2^+ (R31) is the main production path of N atoms. The contribution of R31 decreases rapidly when few more N_2 is added (4% of N_2 has already a drastic effect). This decrease is related to the drastic drop of the electron density shown in figure 10c. The dissociation of N_2 by the metastable argon atoms then becomes dominant between 5 and 55% of N_2 through reaction $Ar^m + N_2 \rightarrow N + N + Ar$ (R28). This matches the experimental data of figure 10b where the density of Ar^m drops when more N_2 is added. The contribution of the dissociation of N_2 by the electrons through $e + N_2 \rightarrow N + N + e$ (R21) becomes comparable to R28 around 55% of N_2 and then dominant at higher N_2 fraction. As displayed in figure 11b, at

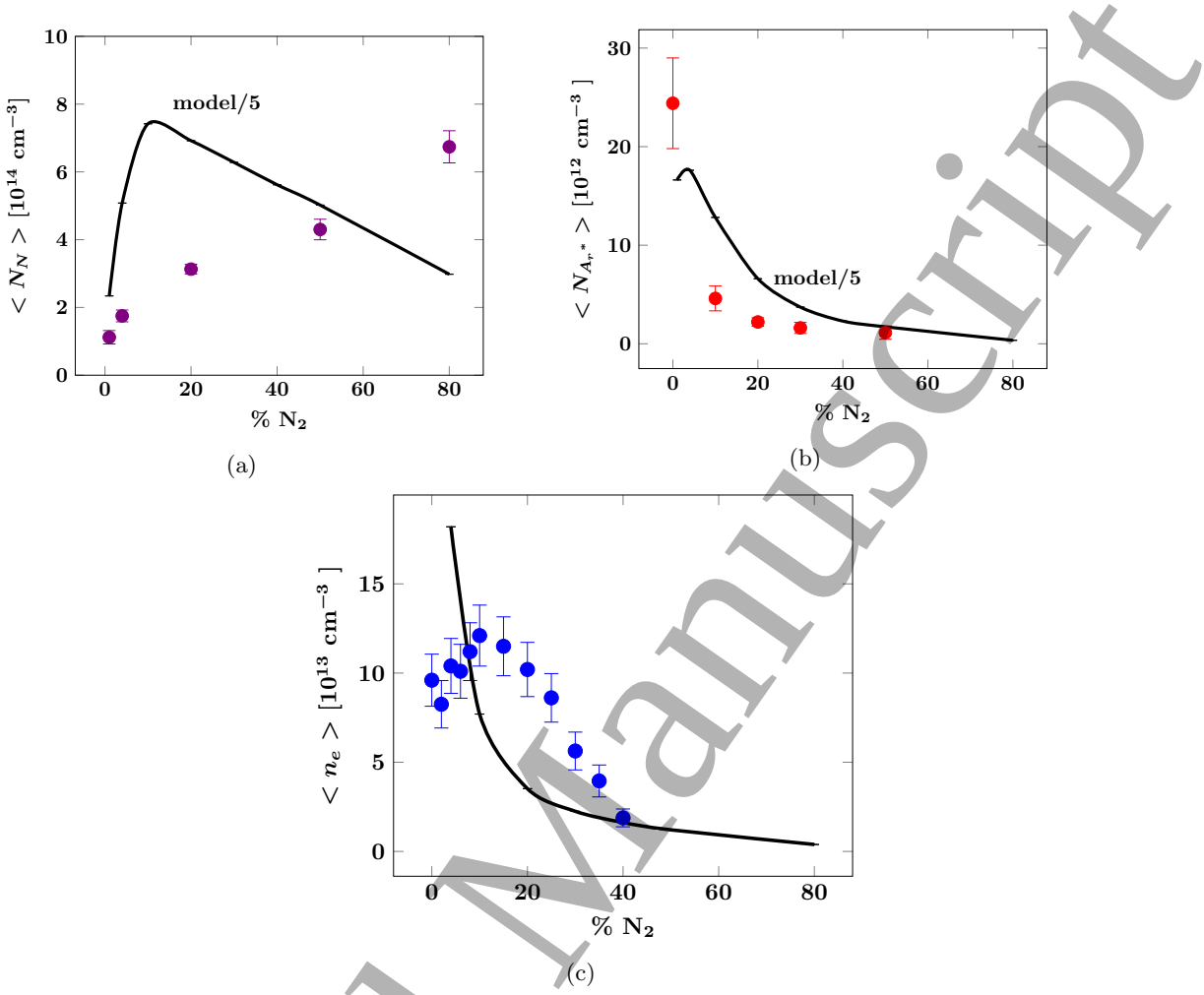

Figure 10: Experimental densities of (a) N atoms, (b) Ar* and (c) e as a function of the percentage of N_2 in the gas mixture. The corresponding calculated densities are also plotted (solid lines). Hole diameter = 0.4 mm, P = 50 mbar, I_d = 1 mA.

low N_2 fraction, the metastable argon atoms are mainly lost through the electron-impact reactions e + Ar^m → Ar^r + e (R9) and e + Ar^m → Ar^{4p} + e (R10). Then, as the electron density decreases, the contribution of these two reactions decreases and, between 30 and 40% of N_2, becomes comparable to the contribution of the quenching reactions R28 and N_2 + Ar^m → N_2(C) + Ar (R56), which are the dominant loss processes of Ar^m at high N_2 fraction. The increase of the N_2(C) vibrational temperature that is expected from R56 has been measured by our team in a similar discharge [51]. The decrease of both the electron and Ar* densities is the reason why the model predicts a decrease of the N atoms density when the N_2 percentage increases (see figure 10a), which is not observed experimentally.

Concerning the density of Ar* presented in figure 10b, its decrease is well captured by the model for N_2 fractions higher than 10%, but it is not the case for the strong experimental variation of the density at low N_2. Moreover, the values of the density predicted by the model are slightly higher than those experimentally measured, as it is also the case for the atomic nitrogen density. This overestimation of the densities by the global model can be partially explained by the fact that the electron energy distribution function (EEDF) is considered as Maxwellian, which is a reasonable hypothesis in pure argon, but it has been recently shown in the literature that the EEDF in Ar/N_2 mixture is not a "Maxwellian-like", exhibiting rather a strong depress at high excitation energy [52].

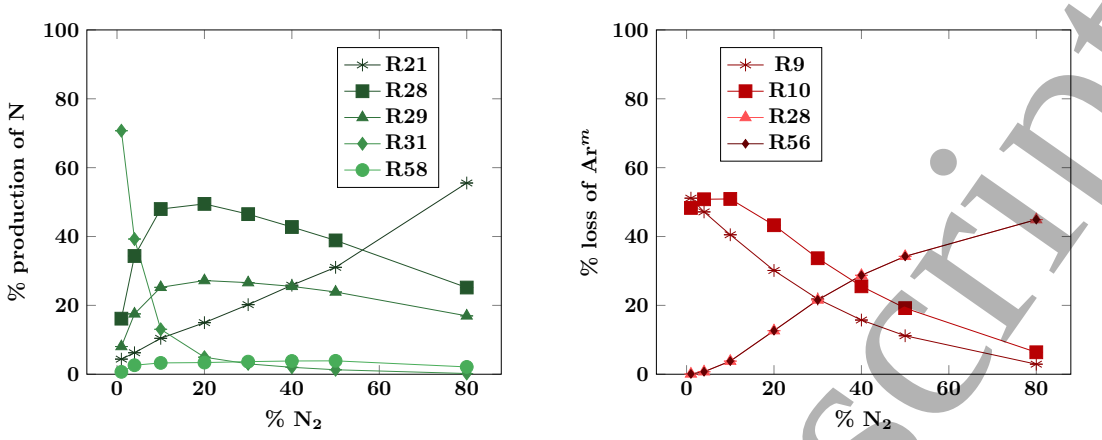

Figure 11: Calculated relative contributions of the non-negligible processes of (a) N atom production and (b) Ar^m loss, as a function of the percentage of N_2 in the gas mixture. Hole diameter = 0.4 mm, P = 50 mbar, I_d = 1 mA.

3.4 N_2 Dissociation Rate

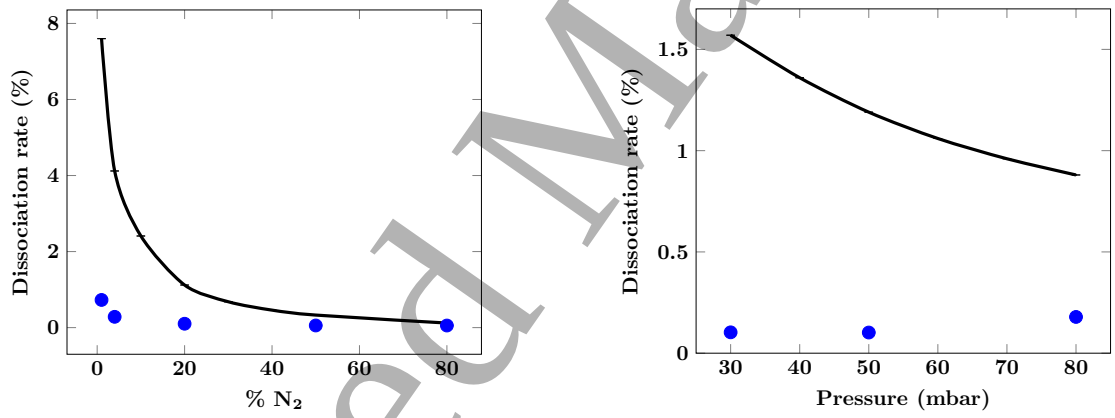

Figure 12: Experimental dissociation rates (blue circle) and the corresponding calculated rates (solid line) as a function of (a) the gas mixture (at P = 50 mbar) and (b) the gas pressure (at 20 % N_2). Hole diameter = 0.4 mm, I_d = 1 mA.

As the absolute density of N atoms is an important parameter for many applications, it is interesting to visualize the efficiency of our discharge at dissociating N_2 molecules. Figure 12 sums up the evolution of the dissociation rate of N_2 as a function of the gas mixture and the pressure. The dissociation rate is defined as $\frac{N_N}{2N^0_{N_2}}$. The evolution of the dissociation rate with the gas pressure and mixture does not change when the hole diameter varies. Hence, only the values for the lowest diameter (0.4 mm), where the dissociation is the greatest, have been plotted.

The measured dissociation rate reaches a few 0.1%, which is lower than what is found in the literature, with dissociation rates of a few percents [53], up to 10 % [18]. Dissociation could be further optimized using a pulsed discharge, as it has been shown to yield greater electronic densities [15]. Note that the experimental decrease of the dissociation rate with the N_2 fraction is well captured by the global model. The larger calculated dissociation rate is related to the larger N atoms density predicted by the model compared to that

measured by FTS absorption.
In figure 12a, one can observe that the N_2 dissociation rate rapidly drops when more N_2 is added to the discharge, from 0.73% to 0.06%. However, we have seen in section 3.3 that this does not translate into a decrease of the N atom density since more N_2 is added. We have seen that the dissociation of N_2 by Ar* (R28), which is dominant between 5 and 55 % of N_2 in the gas mixture, and by electrons (R21), which is dominant at high N_2 fraction, allow a decent dissociation rate to be maintained and a greater N atom density to be achieved (figure 10a). However, R28 does not seem to be efficient at low N_2 percentage, as the question was raised in [54], and is negligible compared to the dissociative electron-ion recombination (R31) in our study. In the model, the contribution of (R28) and (R21) is counterbalanced by the decrease of the electron and Ar* densities beyond 10% of N_2, leading to a decrease of the N atom density, but this is not measured experimentally. As a perspective, a more detailed study above 80% of N_2 would be very interesting to verify if a drop of the N atoms density appears and find the optimal amount of argon admixture in a nitrogen discharge.
Figures 12a and 12b show that the effect of the pressure on the N_2 dissociation rate is much lower than the effect of the gas mixture. However, we can see that the experimental dissociation rate remains constant between 30 and 50 mbar, before slightly increasing at 80 mbar. This is due to the fact that the N atom density increases faster than the increase of N_2 density due to the pressure increase. It should be checked if this effect persists at different N_2 percentages in the gas mixture, when other N atom production reaction dominate.
To optimize the production of N atoms, the experimental data show that a high pressure and high percentage of N_2 is desirable. Nonetheless, we have also noticed that in these conditions, the discharge is less stable and requires a higher electric power from the power supply to operate. This influence the final operating parameters chosen for different applications.

4 Conclusion

In this paper, a MHCD was thoroughly studied by coupling advanced experiments with a 0D volume-averaged model. This study is a step towards the implementation of this plasma source in PECVD reactors and the optimization of the production of nitrogen atoms for nitride deposition on large surfaces. Although the plasma is generated in a small hole, it was demonstrated that it is possible to increase the plasma volume and, thus, the deposition area by: (i) arranging several MHCDs in arrays and (ii) putting a third electrode few centimeters away from the MHCD structure to expand the discharge from the holes to the polarizable substrate [1,51]. The reactive species for the deposition process (in particular nitrogen atoms) are produced in the MHCD hole and that is why it is necessary to understand the fundamental physics of the discharge in this region to optimize the process.

The MHCD was ignited by a DC power supply and operated in the normal regime, in an Ar/N_2 gas mixture. In various experimental conditions, the densities of Ar* and N atoms were determined by absorption spectroscopy (TDLAS and FTS VUV measurements, respectively) and the electron density was obtained by means of high-resolution optical emission spectroscopy. Coupled with a 0D model, these results allow for a better comprehension of the multiple processes involved in the atomic nitrogen production in the MHCD and how it could be optimized to provide efficient nitrogen plasma sources for thin nitride film deposition at lower temperature than conventional CVD. The comparison between the experimental results and the 0D model shows a reasonable agreement with well-captured trends for the different densities but with calculated values of atomic nitrogen and argon metastable atoms densities higher than those given by the experiments. This can be partially explained by the fact that the electron energy distribution function (EEDF) is considered as Maxwellian, which is a reasonable hypothesis in pure argon, but it has been recently shown in the literature that the EEDF in Ar/N_2 mixture is not a "Maxwellian-like", exhibiting rather a strong depress at high excitation energy.
We have found that a smaller hole of the MHCD increases the densities of species, by increasing the power density in the hole. In nitrogen-containing gas mixtures, the applied power to the MHCD is lowered by using a smaller hole, but the power density still rises as well as the density of excited species. It is possible to produce more N atoms by working at a higher pressure, while the Ar* atoms are lost, which could indicate that Ar* is consumed by the dissociation of N_2. A study of the influence of the gas mixture showed that Ar*

compensates the drop of the electron density in gas mixtures between 5 and 55 % of N_2, maintaining some dissociation and yielding a still increasing density of N atoms thanks to the added N_2. A complementary study is needed to check if this effect is maintained for Ar/N_2 gas mixtures with more than 80% of N_2.

Acknowledgments

This work was supported by the French Research National Agency (ANR) through the DESYNIB project (ANR-16-CE08-0004 JCJC) and the Labex SEAM. The authors would like to thank Pascal Chabert and Olivier Guaitella for useful discussions on this work.

References

[1] H. Kabbara, S. Kasri, O. Brinza, G. Bauville, K. Gazeli, J. Santos Sousa, V. Mille, A. Tallaire, G. Lombardi, and C. Lazzaroni. A microplasma process for hexagonal boron nitride thin film synthesis. *Applied Physics Letters*, 116(17):171902, April 2020.

[2] W. Chiang, D. Mariotti, R. M. Sankaran, J. G. Eden, and K. Ostrikov. Microplasmas for advanced materials and devices. *Advanced Materials*, 32(18):1905508, May 2020.

[3] D. Mariotti and R. M. Sankaran. Microplasmas for nanomaterials synthesis. *Journal of Physics D: Applied Physics*, 43(32):323001, August 2010.

[4] C. Yanling, W. Yingkuan, P. Chen, S. Deng, and R. Ruan. Non-thermal plasma assisted polymer surface modification and synthesis: A review. *Biol Eng*, 7(2):1–9, 2014.

[5] J. K. Evju, P. B. Howell, L. E. Locascio, M. J. Tarlov, and J. J. Hickman. Atmospheric pressure microplasmas for modifying sealed microfluidic devices. *Applied Physics Letters*, 84(10):1668, 2004.

[6] J. A. Pérez-Martínez, R. Peña-Eguiluz, R. López-Callejas, A. Mercado-Cabrera, R. A. Valencia, S. R. Barocio, J. S. Benítez-Read, and J. O. Pacheco-Sotelo. An rf microplasma facility development for medical applications. *Surface Coatings Technology*, 201:5684, 2007.

[7] F. Iza, G. J. Kim, S. M. Lee, J. K. Lee, J. L. Walsh, Y. T. Zhang, and M. G. Kong. Microplasmas: Sources, particle kinetics, and biomedical applications. *Plasma Processes Polymers*, 5:322, 2008.

[8] T. Higashiguchi, H. Terauchi, N. Yugami, T. Yatagai, W. Sasaki, R. D'Arcy, P. Dunne, and G. O'Sullivan. Characteristics of extreme ultraviolet emission from a discharge-produced potassium plasma for surface morphology application. *Applied Physics Letters*, 96(131505), 2010.

[9] R. M. Sankaran, K. P. Giapis, M. Moselhy, and K. H. Schoenbach. Argon excimer emission from high-pressure microdischarges in metal capillaries. *Applied Physics Letters*, 83(23):4728–4730, December 2003.

[10] J. Stephens, A. Fierro, B. Walls, J. Dickens, and A. Neuber. Nanosecond, repetitively pulsed microdischarge vacuum ultraviolet source. *Applied Physics Letters*, 104(074105), 2014.

[11] Y. Takao, K. Ono, K. Takahashi, and K. Eriguchi. Plasma diagnostics and thrust performance analysis of a microwave-excited microplasma thruster. *Japanese Journal of Applied Physics*, 45(10):8235–8240, 2006.

[12] K. H. Schoenbach and K. Becker. 20 years of microplasma research: a status report. *The European Physical Journal D*, 70(29), 2016.

[13] K. H. Schoenbach, R. Verhappen, T. Tessnow, F. E. Peterkin, and W. W. Byszewski. Microhollow cathode discharges. *Applied Physics Letters*, 68(13), 1996.

[14] K. H. Schoenbach, A. El-Habachi, W. Shi, and M. Ciocca. High-pressure hollow cathode discharges. *Plasma Sources Science and Technology*, 6(468), 1997.

[15] C. Lazzaroni, P. Chabert, A. Rousseau, and N. Sadeghi. Sheath and electron density dynamics in the normal and self-pulsing regime of a micro hollow cathode discharge in argon gas. *The European Physical Journal D*, 60(3):555–563, December 2010.

[16] D. Z. Pai, K. Ostrikov, S. Kumar, D. A. Lacoste, I. Levchenko, and C. O. Laux. Energy efficiency in nanoscale synthesis using nanosecond plasmas. *Scientific Reports*, 3(1221), December 2013.

[17] Y. Kobayashi, K. Kumakura, T. Akasaka, and T. Makimoto. Layered boron nitride as a release layer for mechanical transfer of gan-based devices. *Nature*, 484(7393):223–227, April 2012.

[18] T. L. Chng, N. D. Lepikhin, I. S. Orel, N. A. Popov, and S. M. Starikovskaia. TALIF measurements of atomic nitrogen in the afterglow of a nanosecond capillary discharge. *Plasma Sources Science and Technology*, 29(3):035017, March 2020.

[19] T. Czerwiec, F. Greer, and D. B. Graves. Nitrogen dissociation in a low pressure cylindrical ICP discharge studied by actinometry and mass spectrometry. *Journal of Physics D: Applied Physics*, 38(24):4278–4289, December 2005.

[20] N. Itagaki, S. Iwata, K. Muta, A. Yonesu, S. Kawakami, N. Ishii, and Y. Kawai. Electron-temperature dependence of nitrogen dissociation in 915 MHz ECR plasma. *Thin Solid Films*, 435:259–263, 2003.

[21] A. Bogaerts. Hybrid monte carlo — fluid model for studying the effects of nitrogen addition to argon glow discharges. *Spectrochimica Acta Part B: Atomic Spectroscopy*, 64(2):126–140, February 2009.

[22] H. R. Griem. *Principle of Plasma Spectroscopy*, volume 2. Cambridge monographs on plasma physics edition, 1997.

[23] C. Lazzaroni, P. Chabert, A. Rousseau, and N. Sadeghi. The excitation structure in a micro-hollow cathode discharge in the normal regime at medium argon pressure. *Journal of Physics D: Applied Physics*, 43(12):124008, March 2010.

[24] C. O. Laux, T. G. Spence, C. H. Kruger, and R. N. Zare. Optical diagnostics of atmospheric pressure air plasmas. *Plasma Sources Science and Technology*, 12(2):125–138, May 2003.

[25] Dirk Spelsberg and Wilfried Meyer. Static dipole polarizabilities of N_2, O_2, F_2, and H_2O. *The Journal of Chemical Physics*, 101(2):1282–1288, July 1994. Publisher: American Institute of Physics.

[26] M. Ivković, S. Jovićević, and N. Konjević. Low electron density diagnostics: development of optical emission spectroscopic techniques and some applications to microwave induced plasmas. *Spectrochimica Acta Part B: Atomic Spectroscopy*, 59(5):591–605, May 2004.

[27] N. de Oliveira, D. Joyeux, D. Phalippou, J. C. Rodier, F. Polack, M. Vervloet, and L. Nahon. A fourier transform spectrometer without a beam splitter for the vacuum ultraviolet range: From the optical design to the first UV spectrum. *Review of Scientific Instruments*, 80(4):043101, April 2009.

[28] N. de Oliveira, D. Joyeux, M. Roudjane, J.-F. Gil, B. Pilette, L. Archer, K. Ito, and L. Nahon. The high-resolution absorption spectroscopy branch on the VUV beamline DESIRS at SOLEIL. *Journal of Synchrotron Radiation*, 23(4):887–900, July 2016.

[29] N. Sadeghi. 6. molecular spectroscopy techniques applied for processing plasma diagnostics. *Journal of Plasma and Fusion Research*, 80(9):767–776, 2004.

[30] K. Gazeli, G. Bauville, M. Fleury, P. Jeanney, O. Neveu, S. Pasquiers, and J. Santos Sousa. Effect of the gas flow rate on the spatiotemporal distribution of $Ar(1s_5)$ absolute densities in a ns pulsed plasma jet impinging on a glass surface. *Plasma Sources Science and Technology*, 27(6):065003, June 2018.

[31] C. Lazzaroni and P. Chabert. A global model of micro-hollow cathode discharges in the stationary regime. *Journal of Physics D: Applied Physics*, 44(44):445202, November 2011.

[32] C. Lazzaroni and P. Chabert. A comparison between micro hollow cathode discharges and atmospheric pressure plasma jets in Ar/O_2 gas mixtures. *Plasma Sources Science and Technology*, 25(6):065015, October 2016.

[33] M. Fiebrandt, B. Hillebrand, S. Spiekermeier, N. Bibinov, M. Böke, and P. Awakowicz. Measurement of Ar resonance and metastable level number densities in argon containing plasmas. *Journal of Physics D: Applied Physics*, 50(35):355202, September 2017.

[34] L. M. Isola, M. López, J. M. Cruceño, and B. J. Gómez. Measurement of the $Ar(1s_y)$ state densities by two OES methods in Ar–N_2 discharges. *Plasma Sources Science and Technology*, 23(1):015014, February 2014.

[35] J. T. Gudmundsson and E. G. Thorsteinsson. Oxygen discharges diluted with argon: dissociation processes. *Plasma Sources Science and Technology*, 16(2):399–412, April 2007.

[36] M. A. Lieberman. Analytical model of atmospheric pressure, helium/trace gas radio-frequency capacitive penning discharges. *Plasma Sources Science and Technology*, 24(2):025009, February 2015.

[37] X. Yuan and L.L. Raja. Computational study of capacitively coupled high-pressure glow discharges in helium. *IEEE Transactions on Plasma Science*, 31(4):495–503, August 2003.

[38] Y. Sakiyama and D. B. Graves. Nonthermal atmospheric rf plasma in one-dimensional spherical coordinates: Asymmetric sheath structure and the discharge mechanism. *Journal of Applied Physics*, 101(7):073306, April 2007.

[39] C. Lazzaroni and P. Chabert. A global model of the self-pulsing regime of micro-hollow cathode discharges. *Journal of Applied Physics*, 111(5):053305, March 2012.

[40] F. Debal, J. Bretagne, M. Jumet, M. Wautelet, J. P. Dauchot, and M. Hecq. Analysis of dc magnetron discharges in Ar- gas mixtures. comparison of a collisional-radiative model with optical emission spectroscopy. *Plasma Sources Science and Technology*, 7(2):219–229, May 1998.

[41] Y. A. Lebedev, T. B. Mavludov, I. L. Epstein, A. V. Chvyreva, and A. V. Tatarinov. The effect of small additives of argon on the parameters of a non-uniform microwave discharge in nitrogen at reduced pressures. *Plasma Sources Science and Technology*, 21(1):015015, February 2012.

[42] M. Touzeau and D. Pagnon. Vibrational excitation of $N_2(C)$ and $N_2(B)$ by metastable argon atoms and the determination of the branching ratio. *Chemical Physics Letters*, 53(2):355–360, January 1978.

[43] N. Kang, F. Gaboriau, S. Oh, and A. Ricard. Modeling and experimental study of molecular nitrogen dissociation in an Ar–N_2 ICP discharge. *Plasma Sources Science and Technology*, 20(4):045015, August 2011.

[44] J. F. Loiseau, P. Pignolet, and B. Held. Numerical simulation of Ar-N_2 excitation transfer in flowing afterglow. *Journal of Physics D: Applied Physics*, 25(5):745–750, May 1992.

[45] H. W. Ellis, R. Y. Pai, E. W. McDaniel, E. A. Mason, and L. A. Viehland. Transport properties of gaseous ions over a wide energy range. *Atomic Data and Nuclear Data Tables*, 17(3):177–210, March 1976.

[46] E. G. Thorsteinsson and J. T. Gudmundsson. A global (volume averaged) model of a nitrogen discharge: I. steady state. *Plasma Sources Science and Technology*, 18(4):045001, July 2009.

[47] J. T. Gudmundsson. The ion energy distribution in a planar inductive oxygen discharge. *Journal of Physics D: Applied Physics*, 32(7):798–803, April 1999.

[48] A. Durocher-Jean, N. Delnour, and L. Stafford. Influence of N_2, O_2, and H_2 admixtures on the electron power balance and neutral gas heating in microwave Ar plasmas at atmospheric pressure. *Journal of Physics D: Applied Physics*, 52(47):475201, September 2019.

[49] K. Ueno, K. Kamebuchi, J. Kakutani, L. Matsuoka, S. Namba, K. Fujii, T. Shikama, and M. Hasuo. Spatially resolved measurements of metastable atom density and electric field strength in a microhollow cathode helium plasma by laser absorption spectroscopy. *Plasma and Fusion Research*, 13(0):3406070–3406070, June 2018.

[50] K. Ueno, K. Kamebuchi, J. Kakutani, L. Matsuoka, S. Namba, K. Fujii, T. Shikama, and M. Hasuo. Spatially resolved laser absorption spectroscopy on a micro-hollow cathode He plasma. *Japanese Journal of Applied Physics*, 58(SA):SAAB03, February 2019.

[51] S. Kasri, L. William, X. Aubert, G. Lombardi, A. Tallaire, J. Achard, C. Lazzaroni, G. Bauville, M. Fleury, K. Gazeli, S. Pasquiers, and J. Santos Sousa. Experimental characterization of a ns-pulsed micro-hollow cathode discharge (MHCD) array in a N_2/Ar mixture. *Plasma Sources Science and Technology*, 28(3):035003, March 2019.

[52] E. Kawamura, M. A. Lieberman, A. J. Lichtenberg, and P. Chabert. Particle-in-cell simulations of the alpha and gamma modes in collisional nitrogen capacitive discharges. *Plasma Sources Science and Technology*, 30(3):035001, March 2021.

[53] M. Tabbal, M. Kazopoulo, T. Christidis, and S. Isber. Enhancement of the molecular nitrogen dissociation levels by argon dilution in surface-wave-sustained plasmas. *Applied Physics Letters*, 78(15):2131–2133, April 2001.

[54] C.-P. Klages, A. Martinovs, L. Bröcker, and D. Loffhagen. Does the energy transfer from Ar(1s) atoms to N_2 lead to dissociation? *Plasma Processes and Polymers*, 17(7):2000070, July 2020.